HAL
open science

Impacts of the Mesoscale Ocean-Atmosphere Coupling on the Peru-Chile Ocean Dynamics: The Current-Induced Wind Stress Modulation

Véra Oerder, François Colas, Vincent Echevin, Sébastien Masson, Florian Lemarié

To cite this version:

Véra Oerder, François Colas, Vincent Echevin, Sébastien Masson, Florian Lemarié. Impacts of the Mesoscale Ocean-Atmosphere Coupling on the Peru-Chile Ocean Dynamics: The Current-Induced Wind Stress Modulation. Journal of Geophysical Research. Oceans, 2018, 123 (2), pp.812-833. 10.1002/2017JC013294 . hal-01661645

HAL Id: hal-01661645

https://inria.hal.science/hal-01661645

Submitted on 12 Dec 2017

HAL is a multi-disciplinary open access archive for the deposit and dissemination of scientific research documents, whether they are published or not. The documents may come from teaching and research institutions in France or abroad, or from public or private research centers.

L'archive ouverte pluridisciplinaire **HAL**, est destinée au dépôt et à la diffusion de documents scientifiques de niveau recherche, publiés ou non, émanant des établissements d'enseignement et de recherche français ou étrangers, des laboratoires publics ou privés.

Climate Dynamics manuscript No.
(will be inserted by the editor)

Impacts of the mesoscale ocean-atmosphere coupling on the Peru-Chile ocean dynamics :

impact of the current-induced wind stress modulation

Vera Oerder · François Colas · Vincent Echevin · Sebastien Masson · Florian Lemarié

Received: date / Accepted: date

V. Oerder
LOCEAN-IPSL, CNRS/IRD/UPMC, UMR7159, Paris, France
Tel.: +33 (1) 44 27 27 11
E-mail: vera.oerder@locean-ipsl.upmc.fr

F. Colas
LOCEAN-IPSL, CNRS/IRD/UPMC, UMR7159, Paris, France

V. Echevin
LOCEAN-IPSL, CNRS/IRD/UPMC, UMR7159, Paris, France

S. Masson
LOCEAN-IPSL, CNRS/IRD/UPMC, UMR7159, Paris, France

F. Lemarié
LJK,INRIA, Grenoble,France

Abstract Keywords XX · XX · XX · XX

1 Introduction

Momentum, heat and water fluxes at the air-sea interface are responsible for intense energy transfers between the atmosphere and the ocean. Processes behind these transfers vary according to the horizontal scales (*e.g.* Xie, 2004). For example, at the basin scale, negative (positive) correlations found by Liu et al (1994) between the SST and the surface wind (solar irradiance, respectively) suggested a forcing of the ocean by the atmosphere, with strong winds and thick cloud cover cooling the underlying water. This contrasts with the observations obtained above smaller scale oceanic structures that suggested an influence of the ocean on the atmosphere. Indeed, satellite data showed an imprint of the oceanic mesoscale ($\sim$ 10-100 km) on the atmospheric fields, in particular on the surface wind stress (*e.g.* Small et al, 2008).

This atmospheric response is created by both the Sea Surface temperature (SST) and the surface current mesoscale anomalies. On one hand, the surface current affects the wind stress ($\overrightarrow{\tau_s}$) because it depends on the relative motion between the ocean and the atmosphere (Dewar and Flierl, 1987), *i.e.* the difference between the absolute surface wind velocity and the oceanic surface current. The intensity of the mesoscale current anomaly can locally be much stronger than the mean current and represent more than 10 % of the surface wind speed (Cornillon and Park, 2001). Consequently, wind stress satellite data show a current-induced mesoscale modulation that represents up to 20 % of the mean wind stress in regions with strong currents like the Gulf Stream (Chelton et al, 2004). In particular, above an oceanic coherent eddy, the wind stress is enhanced on the eddy side where the current's direction is opposite to the wind, and reduced on the eddy side where the current is downwind. This current-induced wind stress anomaly creates a wind stress curl anomaly centered on the eddy (see Fig. 1 from Zhai and Greatbatch, 2007; Gaube et al, 2015).

On the other hand, mesoscale SST anomalies modify the fresh water and heat fluxes at the air-sea interface (Bourras et al, 2004; Frenger et al, 2013) and also affect the wind stress (*e.g.* Chelton et al, 2001) leading to mesoscale anomalies of the wind stress intensity ($\|\overrightarrow{\tau_s}\|'$) proportional to the SST anomalies (SST'). The underlying mechanism may vary with the studied region. For example, in the South East Pacific, it has been shown that these surface wind stress anomalies result from atmospheric vertical mixing modifications due to

SST' (Oerder et al, 2016). Such SST-induced wind stress modulation above SST fronts creates wind stress curl structures proportional to the crosswind SST gradient (Chelton et al, 2001).

Thus, the atmospheric response to the oceanic mesoscale modifies the air-sea exchanges that could further generate a feedback on the mesoscale ocean dynamics. This is the object of the present study. In the present paper, we focus on the current-induced effect, the SST-induced effect being investigated in a companion paper (Oerder et al, 2017).

It has been suggested that the eddies could be directly affected by the wind stress response to the surface current (Dewar and Flierl, 1987). Indeed, in the Southern hemisphere, the negative (positive) wind stress curl observed by Gaube et al (2015) above the warm (cold) anomalies associated with the anticyclones (cyclones) are responsible for an Ekman suction (pumping, respectively) that could damp the eddies.

The oceanic impact of the wind stress modulation by the surface current has been first examined using oceanic models forced by wind stress computed online using a surface wind velocity forcing and the modeled surface current velocity (*e.g.* Zhai and Greatbatch, 2007; Eden and Dietze, 2009; Munday and Zhai, 2015). These studies evidenced a reduction of the mesoscale activity, which is coherent with an eddy damping effect. However, using a forced oceanic model presents a limitation based on the difficulty to obtain a correct absolute surface wind velocity forcing (either from satellite data or from an atmospheric model). Indeed, surface winds derived from satellite data are obtained from an inversion of the wind stress observations inferred from the backscatter of the signal on the ocean surface. Thus, they correspond to a surface wind relative to the moving ocean surface (Cornillon and Park, 2001). In addition, the current-induced wind stress modulation may impact the absolute surface wind velocity through atmospheric boundary layer processes. Current-induced mesoscale variations are not present in wind velocity products (either observed or simulated) with a coarse spatial resolution, nor when the absolute wind is obtained from an atmospheric model which computes the surface stress from the absolute wind only. Besides, a high resolution absolute wind product, either observed or resulting from an atmospheric model (usually forced by remotely-sensed SST), would contain the imprint of the real mesoscale oceanic structures. This oceanic mesoscale (e.g. present in the SST forcing of the atmospheric model) would necessarily differ from the mesoscale structures simulated by the ocean model. Therefore, in both cases, the absolute wind forcing is

not coherent with the oceanic mesoscale. An appropriate way obtain adequate absolute wind conditions at the air-sea interface is thus to use an ocean-atmosphere coupled model. Two recent studies with a regional coupled model in the California Upwelling System (Seo et al, 2015; Renault et al, 2016) take into account the surface current in the wind stress calculation and confirm an impact on the ocean mesoscale revealed by a significant Eddy Kinetic Energy (EKE) reduction.

In the present work, a regional coupled model is configured to simulate the current-wind stress interaction in the South East Pacific and to study its impact on the ocean dynamics. This region hosts one of the most intense Eastern Boundary Upwelling System (EBUS) which are of particular interest because of their intense biological activity (Carr and Kearns, 2003). In EBUS, the mesoscale activity is particularly relevant because it contributes to a large part of the heat transport (Colas et al, 2012) and also structures the nearshore primary production (Lathuilière et al, 2010; Gruber et al, 2011). The upwelling characteristics (nearshore vertical flux, spatial extension of the upwelling zone, etc.) depend on the wind stress intensity and its spatial variations in the coastal zone (Capet et al, 2004). The wind stress also forces an alongshore, equatorward surface coastal current (Strub et al, 1998) with a mesoscale ($\sim$ 150 km) cross-shore extension that could modulate the wind stress intensity and affect the coastal dynamics. As previous studies find a strong impact of the current-stress interaction on the mesoscale activity, we pay a particular attention to the EKE generation mechanisms and the coherent eddies evolution. Our modeling approach allows us to study for the first time the impact on the 3D eddy structure. The methodology is first described in Sec. 2, and the impact on the ocean mean state and mesoscale variability is analyzed in Sec. 3). Then, we focus on the current-wind stress interaction above the simulated coherent eddies (Sec. 4). Finally, we discuss our results and conclude our study in Sec. 5.

2 Methodology

2.1 Regional ocean-atmosphere coupled model

2.1.1 Atmospheric model

The atmospheric dynamics is modeled using the 3.6 version of the Weather Research and Forecasting (WRF) regional model, with the ARW solver (Advanced Research WRF; Skamarock and Klemp, 2008). WRF is based on the fully compressible non-hydrostatic Euler equations with a C-grid and terrain-following mass vertical coordinates. We use the configuration described in Oerder et al (2016) with a 1/12° horizontal resolution. Our domain extends from 10 °N to 30 °S and from 100 °W to 60 °W. The planetary boundary layer physics are parameterized by the Mellor–Yamada–Nakanishi–Niino (MYNN) scheme (Nakanishi and Niino, 2009) and surface fluxes are computed using the MYNN surface scheme. The 3/4° resolution ERA-interim reanalysis (Dee et al, 2011) provides 6-hour averages for the initial and boundary conditions. For further details on the model configuration the reader is referred to Oerder et al (2016).

2.1.2 Oceanic model

The ocean dynamics is modeled using the 3.4 version of the Nucleus for European Modeling of the Ocean (NEMO; Madec, 2008) in a regional configuration with the same 1/12 ° horizontal grid as the atmospheric model. It has 75 z-levels in the vertical, with 25 levels in the upper 100 m. Near the surface, the vertical resolution is 1 m and decreases with depth, reaching 200 m at the bottom. Tracer and momentum horizontal advection is parameterized by an upstream-biased (UBS) third order scheme (Farrow and Stevens, 1995; Webb et al, 1998). A total variance dissipation (TVD) scheme (Lévy et al, 2001) for tracers and a second order centered scheme for momentum are used in the vertical direction. The vertical mixing parameterization is based on a turbulent kinetic energy closure scheme (Blanke and Delecluse, 1993; Madec, 2008). At the open boundaries, the barotropic dynamics is processed using a Flather scheme (Flather, 1976), and relaxation towards boundary values is imposed to the baroclinic fields (Engedahl, 1995). The 1/2° resolution Simple Ocean Data Assimilation (SODA; Carton and Giese, 2008) reanalysis in its 2.1.6 version provides 5-day average boundary conditions

over the 2002-2008 period. An initial state already containing a developped mesoscale circulation is used to reduce the spin-up duration in the coupled simulation. This initial state is obtained from a forced ocean-only simulation over the 2000-2001 period using the NEMO configuration described above. The atmospheric forcing for the spin-up phase is from QSCAT scatterometer (Dunbar et al, 2006) for wind stress and ERA-interim for heat and fresh water fluxes.

2.1.3 Ocean-atmosphere coupling and simulations

The Ocean Atmosphere Sea Ice Sol (OASIS3-MCT, Valcke et al, 2013) coupler is used to couple WRF and NEMO at a 1 h^{-1} frequency as described in Oerder et al (2016). The surface wind stress is computed by WRF in the surface layer scheme using NEMO's surface velocity, and then sent to NEMO through OASIS. Thus, the wind stress fields used by WRF and NEMO are identical (unlike in Seo et al, 2015). Routines in WRF 3.6 (and subsequent versions) were modified (Lemarié, 2015) so that the wind stress ($\overrightarrow{\tau_s}$) can be computed using either the 10 m absolute wind ($\overrightarrow{v_s^a}$) or the 10 m relative wind ($\overrightarrow{v_s^a} - \overrightarrow{v_s^o}$), $\overrightarrow{v_s^o}$ being the surface oceanic current velocity:

$$\overrightarrow{\tau_s} = \rho_a C_d \|\overrightarrow{v_s^a}\|^2 \frac{\overrightarrow{v_s^a}}{\|\overrightarrow{v_s^a}\|} \tag{1}$$

or

$$\overrightarrow{\tau_s} = \rho_a C_d \|\overrightarrow{v_s^a} - \overrightarrow{v_s^o}\|^2 \frac{\overrightarrow{v_s^a} - \overrightarrow{v_s^o}}{\|\overrightarrow{v_s^a} - \overrightarrow{v_s^o}\|} \tag{2}$$

with ρ_a, the surface air density and C_d, the drag coefficient. The drag coefficient C_d is computed in WRF surface scheme using the roughness length and the stability function. Two simulations are compared in the following sections. They are named Abs and Rel, and differ only by the wind stress computation using equation (1) for Abs and (2) for Rel. The simulations are run over the period 2002-2008. The first year is considered the spin-up so results are analyzed over 2003-2008.

2.1.4 Simulation realism and modeled current-stress interaction characteristics

This coupled model configuration has been shown to realistically capture mesoscale air-sea interactions (Oerder et al, 2016). The wind stress modulation by the surface current is characterized by a negative correlation between wind stress curl and surface current vorticity (Chelton et al, 2004; Renault et al, 2016). The wind stress curl $(\overrightarrow{\nabla} \wedge \overrightarrow{\tau_s}) \cdot \overrightarrow{k}$ (hereafter curl($\overrightarrow{\tau_s}$)) presents mesoscale variations induced both by the crosswind projection of the SST anomaly gradient $\mathrm{grad_{cw}}(SST') = \|\overrightarrow{\nabla}(SST')\|\sin(\theta)$ (with θ the counterclockwise angle between $\overrightarrow{\nabla}(SST')$ and $\overrightarrow{\tau_s}$) and by the surface current vorticity. Indeed, curl($\overrightarrow{\tau_s}$) follows the relation (*e.g.* Chelton et al, 2001) :

$$\mathrm{curl}(\overrightarrow{\tau_s}') \propto \mathrm{grad}_{cw}(SST') \tag{3}$$

with a correlation of ~ 0.6 and a regression coefficient $s_1^c = 0.46\ 10^{-2}$ N m^{-2} °C^{-1} (Fig. 1). We estimate the current-induced effect, assuming that the SST and the current-induced effect sum-up linearly, by computing the residual curl ($\mathrm{curl}(\overrightarrow{\tau_s})_{res} = \mathrm{curl}(\overrightarrow{\tau_s}) - s_1^c \mathrm{grad}_{cw}(SST')$) which represents the part of the wind stress curl not proportional to $\mathrm{grad_{cw}}(SST')$. $\mathrm{curl}(\overrightarrow{\tau_s})_{res}$ is negatively correlated (-0.64) to the surface current vorticity (Fig. 1).

A detailed comparison of the modeled and observed, atmospheric and oceanic dynamics in the South East Pacific can be found in Oerder et al (2016). The surface current velocity and wind stress averaged over the 2003-2008 period are shown on Fig. 2. The model (Rel simulation) simulates a coastal equatorward current of 0.1-0.2 m s^{-1}, a well-known characteristic of the South-East Pacific circulation (e.g. Strub et al, 1998). West of 80W, between 5 and 20 S, the offshore current is westward. Its mean intensity is $\sim$ 6 cm s^{-1} in the model, $\sim$ 10 % weaker than the OSCAR product. The modeled wind stress presents a spatially homogeneous bias of $\sim$-0.015 N m^{-2} (it is removed in Fig. 2a for comparison with the observations). It reaches a maximum ($\sim$ 0.2 N m^{-2}) nearshore south of 25 °S and offshore between 20 °S and 5 °S, a pattern also found in the observations. Offshore and south of 25 °S, the modeled wind stress is underestimated by $\sim$ 30 %. In spite of this discrepancy, we consider this simulation realistic enough to carry out a detailed analysis of the simulated mesoscale processes.

2.2 Eddies characteristics

2.2.1 Coherent eddies tracking

Coherent oceanic eddies are detected using 1-day average surface fields, following the method described by Kurian et al (2011), and used by Colas et al (2012) and Liang et al (2012). This method is based on closed contours identification of the Q parameter, the second invariant of the horizontal velocity gradient tensor (Isern-Fontanet et al, 2003). Closed contours are fitted by circles and a shape error is defined as the closed-contour area deviation from the circle area. Coherent eddies are defined as the largest circular (*i.e.* shape error $< 20\%$) closed-contours fitted by a circle with a radius ranging from 40 km to 120 km. The eddy center and radius are those of the fitted circle. Eddies are tracked by comparing eddy centers and properties between consecutive times. The nearest eddies with the minimum change in amplitude and surface are assigned to common tracks. Only eddies detected for at least 15 days are retained for the analysis.

2.2.2 Composites

To study coherent eddies characteristics, composites of the sea temperature anomaly associated to cyclones and anticyclones are computed using the following methodology. For each eddy detected on daily-averaged field, temperature anomalies relative to a 90-day running mean are calculated. The mean surface wind direction above the eddy is also computed using a 90-day running mean. The temperature anomaly field is then rotated around the eddy center, so that the mean wind direction is South-North for each eddy. Zonal and meridional axes are rescaled so that the eddy radius is equal to the averaged cyclone or anticyclone radius. Finally, all temperature anomaly fields are averaged to create the composite eddy. The same method is applied for the current velocity and vorticity.

3 Impacts of the current-stress interaction on the ocean dynamics

The Abs and Rel simulations are compared to investigate the ocean response to the current-stress interaction. We first examine the impact of this process on the ocean mean state, and then on mesoscale variability by quantifying the impact on the eddy kinetic energy (EKE) and its generation terms.

3.1 Regional circulation

Offshore of a $\sim$ 400-km-wide coastal band, between the equator and 30°S, the differences in the large-scale fields are weak. The observed and modeled mean SST differ by less than 0.2 °C, and the wind stress by less than 0.2 % (not shown). In the nearshore region, the surface wind $\overrightarrow{v_s^a}$ is weaker ($\sim$ 5 m s^{-1}) than offshore and the mean surface current is stronger ($\sim$ 20 cm s^{-1}). As both the surface wind and the surface current are alongshore and equatoward, we could expect the wind stress computed from the relative wind (Rel) to be weaker than the wind stress computed from the absolute wind (Abs). A wind stress is calculated offline using Abs surface fields (surface wind and current) and following equation (2). Between 7 °S and 13 °S, this offline wind stress is up to 8 % weaker than the Abs wind stress computed online (Fig. 3a). One could expect a similar difference between Rel and Abs wind stress, however, it is much weaker (<3 %). This is due to a partial compensation of the wind stress weakening in Rel by a stronger surface wind (up to 3 % stronger, not shown).

Due to the weak modification of the alongshore wind stress (Fig. 3a), the mean oceanic circulation is virtually unchanged. The modeled poleward undercurrent is consistent with *in situ* ADCP observations (Chaigneau et al, 2013). It extends between 30 m and 230 m depth and between the coast and 150 km offshore (Fig. 3b), as in the observations albeit with a weaker intensity. The mean current velocities differ by less than 2 cm s^{-1} in the simulations (Fig 3c). The isotherms shoaling near the coast (Fig 3b), characteristic of the upwelling, is well reproduced by the model. The thermal structure is barely modifed by the coupling, with differences less than 2 % (Fig 3c).

3.2 Eddy Kinetic Energy

We now focus on the impact on the mesoscale activity. Both simulations show a depth-integrated EKE minimum nearshore (Figs. 4a-c), two maxima (north of 18°S, between $\sim$ 50 and 300 km from the coast, and south of 26°S) which is consistent with estimations of surface EKE from observations (*e.g.* Colas et al, 2012; Oerder et al, 2015). The EKE is maximum at the surface and decreases with depth (Fig. 4d). Its structure changes with the distance from the coast: it decreases offshore in the surface layer (above 50 m depth) and increases in the subsurface (Fig. 4d). This indicates a "barotropization" of the eddy kinetic energy related to the inverse energy cascade of the eddies moving offshore (*e.g.* Haney et al, 2001; Colas et al, 2013).

The integrated EKE is weaker in Rel than in Abs both nearshore (-15 % within 200 km from the coast) and offshore (-20 % between 200 and 500 km). The EKE reduction is stronger near the surface: the mean surface EKE is reduced by $\sim$ 30 % over the first 500 km (Fig. 4c). Vertical profiles shows that the EKE difference between the two simulations reduces with depth. However, as a consequence of the eddy energy "barotropization", this difference at depth increases with offshore distance: at $\sim$ 150 m depth, it is 2.3 stronger 400 km from the coast than 100 km from the coast (Fig. 4d). Interestingly, this leads to a slightly more barotropic EKE in Rel than in Abs.

3.3 EKE production

To explain the EKE reduction due to the current-stress interaction, the main conversion terms contributing to the depth-integrated EKE generation are analyzed (*e.g.* Marchesiello et al, 2003):

$$F_e K_e = \frac{1}{\rho_0}(\overline{u'(z=0)\tau'_x} + \overline{v'(z=0)\tau'_y}) \tag{4}$$

$$K_m K_e = -\int_Z^0 (\overline{u'u'}\frac{\partial \overline{u}}{\partial x} + \overline{u'v'}\frac{\partial \overline{u}}{\partial y} + \overline{u'w'}\frac{\partial \overline{u}}{\partial z} + \overline{v'u'}\frac{\partial \overline{v}}{\partial x} + \overline{v'v'}\frac{\partial \overline{v}}{\partial y} + \overline{v'w'}\frac{\partial \overline{v}}{\partial z})dz \tag{5}$$

$$P_e K_e = -\int_Z^0 \frac{g}{\rho_0}\overline{\rho' w'} \tag{6}$$

with $\bar{\cdot}$ the temporal average and $\cdot'$ the anomaly relative to the temporal average. u, v and w are the zonal, meridional and vertical velocities, ρ is the water density, ρ_0 is a reference density (mean water density), and τ_x and τ_y are the zonal and meridional wind stress. P_eK_e represents the energy transfer from eddy potential energy to EKE (baroclinic conversion), and K_mK_e is the transfer from mean kinetic energy to EKE (barotropic conversion). F_eK_e corresponds to the EKE creation by the wind stress anomalies. These terms are computed from 5-day-average model outputs. Anomalies $\cdot'$ are defined relatively to a 90-day running mean.

The EKE generation mainly occurs in a $\sim$ 200-km wide coastal strip, with a maximum located 75-100 km offshore (Fig. 5). This is consistent with previous studies using forced-ocean simulations in the South-East Pacific (Belmadani et al, 2012) and the California (Marchesiello et al, 2003) regions. 70 % of the total EKE generation is due to P_eK_e within 200 km from the coast (Fig. 5a). There, the vertical shear of the alongshore velocity generated by the equatorward surface current and the poleward undercurrent (Fig. 3b) leads to baroclinic instabilities, converting potential energy to EKE (Colas et al, 2012). The K_mK_e cross-shore profile shows that eddies transfer energy to the alongshore mean flow ($K_mK_e < 0$) within 50 km from the coast. Between 50 and 150 km offshore, barotropic instabilities transfer kinetic energy from the mean coastal currents to EKE ($K_mK_e > 0$). This transfer represents $\sim$ 15 % of the total EKE generation (Fig. 5b). As the two other terms, F_eK_e is maximum near the coast, where the current anomalies are largest (Fig. 5c). It contributes to $\sim$ 25 % of the EKE generation within 200 km from the coast.

Overall, the total EKE generation (i.e. $F_eK_e + K_mK_e + P_eK_e$) is 30 % weaker in Rel than in Abs in a 200-km-wide coastal band. This reduction is mainly due to a weakening of F_eK_e (Fig. 5c). This is consistent with Duhaut and Straub (2006), who showed that the wind stress work computed with a relative wind (Eq. 2) is always smaller than the one computed with absolute surface wind (Eq. 1). It is generally considered that the main wind work contribution to the ocean circulation is the wind work associated with the geostrophic current (*e.g. Wunsch, 1998)* :

$$F_eK_{eg} = \frac{1}{\rho_0}(\overline{u'_g(z=0)\tau'_x} + \overline{v'_g(z=0)\tau'_y}) \tag{7}$$

with u_g and v_g the zonal and meridional geostrophic velocities, respectively. Indeed, the wind work on ageostrophic currents can be approximated by the work on Ekman currents that is dissipated through vertical turbulence in the Ekman layer, and, thus, it does not contribute to the ocean circulation (Wang and Huang, 2004). Our results show that ∼90 % of the $FeKe$ reduction is attributed to the $FeKeg$ reduction (Fig. 5c). Note that $FeKeg$ and $FeKe$ are negative in Rel offshore of 75 km from the coast, indicating an EKE dissipation by the wind work.

The averaged differences (from the coast to 500km offshore) in K_mK_e (0.03 cm^3 s^{-3}) and P_eK_e (0.04 cm^3 s^{-3}) between the two simulations are much smaller than in F_eK_e (0.18 cm^3 s^{-3}). P_eK_e is, on average, increased by 0.02 cm^3 s^{-3} (10 % of the total change in EKE generation) in Rel between 50 - 100 km from the coast, and reduced by 0.08 cm^3 s^{-3} (30 %) between 100 and 200 km offshore ((Fig. 5a). Note that a longer simulation period would be necessary to ensure the robustness of these values.

In summary, the main impact of the current-stress interaction is to reduce the surface and depth-integrated EKE by 30 % and 20 % respectively. This EKE reduction can partly be attributed to a 30 % weakening of the EKE sources in the coastal region. A part can also be due to the fact that mesoscale structures, created nearshore through instabilities of the alongshore current system, evolve differently during their lifetime under the action of this air-sea interaction. To investigate this issue, we now analyze the coherent eddies detected in the simulations.

4 Impacts on the coherent eddies

To examine the impact of the current-stress interaction on the coherent eddies, we first compare the eddy characteristics (Sec. 4.1) before studying the processes responsible for the differences between the two simulations (Sec. 4.2).

4.1 Eddies characteristics

In both simulations, the cyclones and anticyclones have the same mean radius (differences are less than 2 %; Table 1) and cyclones have a longer lifetime (∼ 20 %) than anticyclones. The mean eddy lifetime is ∼ 15 %

shorter in Rel than in Abs, which can be related to an eddy damping by the current-wind stress interaction. This shorter lifetime may explain why fewer eddies ($\sim$ 10%, Table 1) were found in Rel as part of short-lived ($\lesssim$ 20 days) eddies population in Abs may have its lifetime becoming smaller than the detection threshold (15 days; Sec. 2.2.1) in Rel.

More anticyclones ($\sim$ 10 %) than cyclones are found in Abs. This is at odds with estimations from satellite altimetry (Chaigneau et al, 2008, 2009; Pegliasco et al, 2015) which do not find a significative difference between the number of cyclones and anticyclones in the South East Pacific. The asymmetry in the cyclones-anticyclones number is reduced in Rel ($\sim$ 3%, Table 1), indicating a more realistic eddy distribution. This is related to the fact that there are more (179) short-lived (<20 days) anticyclones than cyclones in Abs and the lifetime reduction in Rel makes an important part of these eddies undetected. As a result, the eddy number diminution between Abs and Rel is larger for the anticyclones (277) than for the cyclones (127).

The cyclonic cores are located near the surface while the anticyclones can be separated in two categories according to their core depth (at surface or subsurface; Colas et al, 2012; Pegliasco et al, 2015). An anticyclone is considered a surface eddy when its temperature anomaly maximum is located above 100 m depth. Half of the detected anticyclones are subsurface eddies. Note that some of the subsurface anticyclones having a weak signature at the surface may not be detected as our method is based on the surface current fields. However, in the context of the present study, we do not see this as a limitation as eddies with a very weak surface current signature do not interact strongly with the atmosphere. 159 (118) fewer surface (subsurface) anticyclones are found in Rel than in Abs. Again this difference is likely attributed to the longer lifetime ($\sim$ 30 %) of subsurface anticyclones compared to the surface ones.

To investigate further the eddy differences between the simulations, we now analyze their 3D structures. Composites of the temperature anomaly are shown in Fig. 6. Cyclones are associated with a cold anomaly reaching a minimum at $\sim$ 150 m depth (Figs.6a,d), which is consistent with observations (Chaigneau et al, 2011). In Rel, the cyclones temperature anomaly is reduced by $\sim$ 10 % at the surface and $\sim$ 30 % at the core depth (Fig.6g). Below 150 m, the difference between the two simulations decreases with depth. The surface anticyclones present positive temperature anomaly at all depths, with a maximum around 50 m depth (Figs.6b,e).

In contrast, the subsurface anticyclones are characterized by a cold anomaly in the near-surface and a warm anomaly (Figs.6c,f) reaching a maximum around 400 m (in agreement with Pegliasco et al, 2015).

As for cyclones, the surface anticyclones anomaly reduction in Rel is weak at the surface ($\sim$ 5 %) and reaches a maximum at the eddy core depth ($\sim$ 45 % at 100 m depth; Fig.6h). Interestingly, the situation is different for the subsurface anticyclones (Fig.6i). In Rel, their anomaly is cooler at all depths, leading to an intensification (by $\sim$ 35 %) and a deepening (down to $\sim$ 100 m) of the near-surface cold anomaly. Below, as for the surface anticyclones, the warm anomaly is significantly reduced in the depths range of the eddy core (-55 % at 150 m depth).

The vorticity anomaly structure shows a maximum intensity near the surface for the three eddy types (Fig. 7). This is consistent with the eddy vorticity composites in Colas et al (2012). In Abs, the surface vorticity anomaly is stronger for the surface anticyclones and the cyclones ($\sim$-0.14 and $\sim$0.12, respectively) than for the subsurface anticyclones ($\sim$-0.095). The vorticity anomaly extends deeper in the subsurface anticyclones: anomaly stronger than 0.04 reaches 400 m depth, while it goes to 200 m depth in the surface anticyclones and 250 m depth in the cyclones. In Rel, vorticity anomalies are $\sim$ 30-35 % weaker for all eddy types in the surface layer (0-50 m depth). This difference decreases abruptly below: at 400m depth, the vorticity anomaly is reduced by $\sim$10-15 %. The surface anticyclones still have a stronger surface vorticity anomaly than the subsurface ones but by only $\sim$ 20 % (Fig.7b,c). In contrast, at 400 m depth, the vorticity anomaly in the subsurface anticyclones is $\sim$40% larger than in the surface ones.

Overall, both the temperature and vorticity anomalies associated to the eddies are reduced under the action of the current-stress coupling. This reduction is stronger around 100-150 m depth for the temperature and near the surface for the vorticity.

4.2 Current-induced stress anomalies effect

The eddy damping effect due to the current-stress interaction reduces the eddies intensity and shortens their averaged lifetime by 15 %. To further investigate this effect, we now focus on the eddies with a lifetime longer than 40 days. We first examine the temporal evolution of the eddy surface characteristics (Fig. 8). The eddy

amplitude is derived from the sea surface height (SSH) anomaly following Chaigneau et al (2008), Samelson et al (2014) and Pegliasco et al (2015). Cyclones (anticyclones) amplitude is $\sim$ 20 % (10 %, respectively) weaker in Rel on the first day of detection. This is likely due to the action of current-stress interaction on the eddy structure during its early life phase, before it is actually detected as a coherent eddy. To better compare the eddy evolution in Abs and Rel, we normalize the eddy amplitude by its first day value. The eddy evolution is divided in two periods: growth during the first $\sim$ 25 days, and decay after (Fig. 8a). This is consistent with Samelson et al (2014) and Pegliasco et al (2015) who distinguish an eddy growth phase during the first half of its lifetime and a decay phase in the second half. Both the growth and decay phases are affected by the current-stress interaction in Rel. For the cyclones (anticyclones), the growing is reduced by $\sim$ 15 % ($\sim$ 25 %, respectively). The decay is $\sim$ 50 % stronger for both cyclones and anticyclones. As a result, after 40 days the eddy amplitude is $\sim$ 10 % weaker in Rel. Thus, not only the coherent eddies are weaker in Rel than in Abs at their initial detection, but they are also clearly damped during their entire lifetime

This contrasts with Renault et al (2016) who suggest no impact of the current-stress interaction on growth and decay phases, while during a "mid-life phase" the coupling process is responsible for a slow decay. This discrepancy may be due to their choice to normalize the time axis for the eddy evolution, so that changes in the eddy lifetime are not taken into account.

The surface amplitude evolution of the surface and the subsurface anticyclones has also been compared (not shown). For both anticyclones types, eddy damping is consistently stronger in Rel.

The eddy damping also impacts the mean surface vorticity (Fig 8b). After 40 days, the cyclones (anticyclones) vorticity are $\sim$ 5 % (12 %, respectively) weaker in Rel.

Previous studies suggested that two dynamical processes can explain the eddy damping by the current-stress interaction: wind work (*e.g.* Zhai and Greatbatch, 2007) and Ekman pumping (*e.g.* Dewar and Flierl, 1987). We first focus on the role of the wind work F_eK_{eg}. We showed that, near the coast (within a 75 km band) the wind work transfers eddy kinetic energy from the atmosphere to the ocean, whether or not current-stress interaction is taken into account (Sec.3.3 ; Fig. 5c). On the other hand further offshore (from $\sim$ 75 km), F_eK_{eg} exhibits

ubiquitous negative values in Rel, which corresponds to an EKE sink. To better understand this mechanism, we construct composite average above coherent eddies in Abs (Fig. 9) and in Rel (Fig. 10). In Abs, a wind stress anomaly is created above the eddies. It is only due to the SST anomaly following the relation:

$$\|\overrightarrow{\tau_s}\|' \propto SST' \tag{8}$$

with a very high correlation of 0.97 (0.88) for negative (positive) wind stress anomaly above the cyclones (anticyclones, respectively; Figs. 9a-d). A more detailed study of the mesoscale SST-induced wind stress response is presented in (Oerder et al, 2017). **XXX (PB REF ICI) XXX** It can be noted that, over both cyclones and anticyclones, the wind stress anomaly is along (opposed) the current anomaly on the right (left) side of the eddy.As a consequence, (F_eK_{eg}) is necessarily positive (negative) on the right (left) side of the eddy (Fig. 9c,d). This is confirmed by examining the composites (Figs.9e,f): wind work tends to inject energy on the right side and to dissipate it on the left side.

In Rel, the wind stress is affected by the SST and the current mesoscale anomalies. The wind stress anomaly composites (Fig.10a,b) display very different patterns than in Abs. A bilinear regression shows that the composites follow the relation

$$\|\overrightarrow{\tau_s}\|' = s_1^\tau SST' - s_2^\tau \overrightarrow{v_g}' . \frac{\overrightarrow{\tau_s}}{\|\overrightarrow{\tau_s}\|} \tag{9}$$

with high correlation of 0.99 for the cyclones and 0.97 for the anticyclones. The regression coefficients are s_1^τ =6.8 (7.9) 10^{-3} N m^{-2} °C^{-1} and s_2^τ =1.2(0.6) 10^{-2} N s m^{-2} m^{-1} for the cyclones (anticyclones, respectively). The wind stress direction is largely altered by the surface current (Figs.10a,b) that tends to create a wind stress gyre in an opposed sense of rotation than the eddy (*e.g.* Cornillon and Park, 2001). The composite above cyclones (Fig.10a) shows that the current-induced effect on the wind stress direction dominates the SST-induced effect. As the wind stress anomaly above cyclones is clearly an anticyclonic gyre, F_eK_{eg} is expected to be negative all over the eddy rim (Fig. 10c), which is confirmed by the composite (Fig. 10e).

Results above anticyclones are slightly different. The wind stress anomaly composite has a positive curl, as the current-induced effect creates a cyclonic wind stress gyre (Fig.10b). However, the positive SST anomaly creates

a wind stress anomaly in the wind current direction (Fig. 9a) which strengthens the current-induced wind stress on the eddy left side and weakens it on the right side. As a result, the total stress anomaly almost vanishes on the right side (Fig.10b). The wind stress cyclonic gyre created by the current should theoretically induce a negative F_eK_{eg} on both sides of the anticyclonic eddy (Fig. 10d). This contrasts with the F_eK_{eg} composite (Fig. 10f) that has a negative pattern on the left side only. On the right side, the SST-induced effect compensates the current-induced effect. Note that removing the SST effect by substracting the patterns in Fig. 9f and 10f consistently results in a negative wind work over both eddy sides (not shown). Overall, our results show a very different action of the wind work on the coherent eddies when the current-stress interaction is taken into account: the wind work always dissipates energy above the eddies and thus actively contributes to damp them.

We now turn to the impact of the eddy-induced Ekman pumping on the eddy damping. In Abs, eddy-induced wind stress variations (Fig 9a,b) create a wind stress curl and an Ekman pumping anomaly proportional to $\mathrm{grad}_{cw}(SST')$ (Fig 11a,b). Correlations between the Ekman pumping and $\mathrm{grad}_{cw}(SST')$ composites are 0.95 and 0.88, with a regression coefficient of -0.15 and -0.19 m^2 s^{-1} °C^{-1} for the cyclones and anticyclones, respectively. Consequently, the SST-induced Ekman pumping corresponds to a dipole (Fig 11a,b) with upwelling on the left (right) side of the cyclone (anticyclone) and downwelling on the right (left) side of the cyclone (anticyclone). The corresponding vertical velocities do not exceed 6.5 cm day^{-1}. In Rel, Ekman pumping anomalies W'_{Ek} result from the superposition of the two effects, following the relation:

$$W'_{Ek} = s_1^{Ek}\mathrm{grad}_{cr}(SST') - s_2^{Ek}\mathrm{curl}(\overrightarrow{v_o}) \tag{10}$$

with s_1^{Ek} =-0.085 (0.14) m^2 s^{-1} °C^{-1}, s_2^{Ek} =2.10^{-4} (3.10^{-4}) m^{-1} for cyclones and anticyclones, respectively. A correlation of 0.98 between the left and right terms of equation (10) is found for both cyclones and anticyclones. W'_{Ek} composites in Rel (Fig 11c,d) are dramatically different from those in Abs (Fig 11a,b). Anomalies in Rel are centered on the composite eddy, indicating that the current-induced Ekman pumping ($-s_2^{Ek}\mathrm{curl}(\overrightarrow{v_o})$) is overwhelmingly dominating the SST-induced effect. The corresponding vertical velocity reaches 16 cm day^{-1}.

The current-stress effect also induces subsurface vertical velocities within the eddy core (Fig. 12). The mean vertical velocity (between 0 and 400 m depth) is 90 % (65 %) stronger in Rel than in Abs in the cyclones (anticyclones, respectively). The Ekman downwelling (upwelling) in the cyclones (anticyclones) is responsible for the enhanced damping of the cold (warm) temperature anomaly in Rel (Fig. 6). Note that the vertical circulation anomaly induced by the Ekman pumping is stronger around 50-100 m depth (Fig. 12), which could explain why the eddy temperature damping is stronger at depth than at the surface (Fig. 6).

5 Discussions and conclusion

We study the impact of the wind stress-surface current coupling on the mesoscale circulation by comparing two coupled simulations that differ by their surface wind stress computation: using the absolute surface wind velocity (Abs) or the relative surface wind velocity (Rel). The regional ocean circulation is almost unchanged because the surface absolute wind velocity is modified in Rel in such a way that the mean wind stress remains very similar in both simulations. Nevertheless, the surface EKE is reduced by ~ 30 % in Rel with respect to Abs. This reduction is due to a weakening of the coastal EKE generation (through a decrease of the wind work) and a more efficient offshore damping of coherent eddies in Rel. The eddy damping results from energy dissipation by the wind work and eddy-induced Ekman pumping.

5.1 Impact on the mean circulation and eddy kinetic energy

The mean coastal ocean currents in the South East Pacific differ by less than 2 cm s^{-1} between Abs and Rel because of the unchanged mean wind stress. These results are consistent with contemporary studies in the California Current System (CCS) showing little impact on the mean regional circulation (Seo et al, 2015; Renault et al, 2016). However, the impact on the mean circulation may be stronger in other regions with much stronger currents where wind stress modulations by surface current were clearly evidenced (Chelton et al, 2004). Yet there is an ubiquitous EKE reduction, due to the current-stress interaction, that is comparable to those obtained for the CCS (surface EKE reduced by 42 % in Seo et al (2015) and integrated EKE reduced by 27

% in Renault et al (2016)). Examining the EKE generation terms in the nearshore region, we find a significant decrease of the energy input by the wind work and indistinguishable modifications of P_eK_e and K_mK_e when the current-stress interaction is active. This is consistent with Renault et al (2016) but contrasts with the increase in P_eK_e in Seo et al (2015).

The strong impact of the current-stress interaction on the EKE intensity calls for a better representation of this effect in ocean simulations. The computational cost of a high-resolution ocean-atmosphere coupled models over large domains remains very high, so alternative approaches need to be found for ocean-forced simulations. Several studies attempted to simulate this effect by using a surface wind velocity forcing to compute a wind stress (following equation 2, Sec. 1). These works show an EKE reduction from 10 % (Zhai and Greatbatch, 2007) to 50 % (Eden and Dietze, 2009) with F_eK_e decreasing from 17 % (Zhai and Greatbatch, 2007) to 35 % (Duhaut and Straub, 2006), which is consistent with our results. However, in the coastal region, we show that, for a given fixed absolute wind velocity, the wind stress reduction using Eq.(2) instead of (1) is much higher (up to 8%) than in a coupled framework (less than 3 %). This indicates that using (2) in a forced ocean model would lead to unrealistic ocean dynamics. In an attempt to mimic the current-induced wind velocity modulation in an oceanic forced simulation, Renault et al (2016) suggest to modify the computation of the wind stress (Eq. 2) following the relation : $\overrightarrow{\tau_s} = \rho_a C_d \|\overrightarrow{v_s^a} - (1-s_w)\overrightarrow{v_1^o}\|^2 \frac{\overrightarrow{v_s^a} - (1-s_w)\overrightarrow{v_1^o}}{\|\overrightarrow{v_s^a} - \overrightarrow{v_1^o}\|}$. s_w is determined by examining the wind velocity response to the surface current anomalies in a coupled ocean-atmosphere simulation. This method presents several limitations. First, it requires to run a preliminary coupled simulation to estimate s_w, and this has an important computational cost. Second, it ignores a possible dependency of the current-induced wind velocity modulation from the atmospheric model parameterizations. Last, it assumes that s_w is constant in time and space. Therefore, adequately representing the modulation of the surface wind conditions by the oceanic mesoscale without using a fully coupled model remains an open question.

5.2 Impacts on the coherent eddies

Our results show that the mesoscale-induced wind stress variations above the coherent eddies can be approximated by the linear superposition of the SST-induced and the current-induced effects (Eq. 9). The term

$s_1^\tau SST' \sim 10^{-3}$ N m^{-2} is dominant compared to $s_2^\tau \overrightarrow{v_g}' . \frac{\overrightarrow{\tau_s}}{\|\overrightarrow{\tau_s}\|} \sim 3.10^{-4}$ N m^{-2}, which explains why relation (8) is clearly identified in the South-East Pacific (Oerder et al, 2016) and other regions (e.g. O'Neill et al, 2010b). On the other hand, the current-stress interaction has a stronger impact on the wind stress direction, leading to a larger wind stress curl anomaly above eddies than the SST-induced effect. We show that the term $s_1^{Ek}\mathrm{grad}_{\mathrm{cw}}(SST')$ is 2.5 times weaker than the term $-s_2^{Ek}\mathrm{curl}(\overrightarrow{v_o})$ (6.5 cm day^{-1} and 16 cm day^{-1}, respectively). This is consistent with Gaube et al (2015) showing a SST-induced Ekman pumping being two to three times weaker than the current-induced Ekman pumping. Note that the wind stress divergence is little affected by the current-induced effect (not shown). This might explain why correlations between the wind stress divergence and the downwind SST gradient are always higher than the correlations between wind stress curl and cross-wind SST gradient (relation 3, O'Neill et al, 2010a).

Above cyclones, the current-induced effect on the wind stress direction is largely dominant compared to the SST effect, and it generates a clear wind stress anticyclonic anomaly. Above anticyclones, the relative importance of the two effects is somewhat different. The SST-induced wind stress modification, that strengthens (weakens) the current-induced wind stress anomaly on the left (right, respectively) side of the eddy, compensates almost totally the current effects on the right side of the eddy (Fig. 10b). Two reasons might explain why the SST-induced effect is more important for the anticyclones. First, the surface current anomaly is on average stronger for cyclones than for anticyclones because many of the latter are subsurface eddies with deep cores. Second, the regression coefficient s_2^τ is twice stronger for the cyclones than for the anticyclones, while s_1^τ is almost unchanged. This indicates that, for a given intensity of the surface current anomaly, the current-induced effect on the wind stress is twice stronger in the case of cyclones. Understanding the mechanisms driving this asymmetric response is beyond the scope of our study.

Overall, the wind stress response to the mesoscale currents is responsible for an eddy damping that occurs during the entire eddy lifetime through an enhanced Ekman pumping and a negative wind stress work. The F_eK_{eg} composites (Fig. 10) show indeed that the wind work due to the current-stress interaction is negative everywhere above the eddies (unlike what is stated in Renault et al, 2016). It seems quite logical since the

current-induced wind stress anomalies are always opposed to the current anomalies on both sides of the eddies (see schemes in Figs.10c,d).

5.3 Implications for the South East Pacific

In the South-East Pacific, mesoscale eddies are responsible for a significant fraction of the heat advection (Colas et al, 2012). Thus the mesoscale activity modulation induced by the current-stress interaction may affect the regional heat balance. Following Chaigneau et al (2011) and using the temperature anomaly composites presented in Fig.6, we estimate the available heat anomaly transported by the composite coherent eddies. We found heat anomalies of -3.1 10^{18} J (-1.5 10^{18} J) for cyclones and 2.5 10^{18} J (1.6 10^{18} J) for anticyclones in Abs (Rel, respectively). Based on the eddy census in Abs and Rel, we can crudely approximate that the contribution of coherent eddies to the heat transport is reduced by at least 50 % by the current-stress interaction. Note that an accurate estimate of the coherent eddies contribution to the total eddy heat transport ($\sim$ 20-35 %, Colas et al, 2012) is difficult to achieve. A dedicated study would be required to quantify precisely the overall effect of the current-stress interaction on the regional heat balance.

This effect on the mesoscale dynamics could also modulate the intense biogeochemical activity in the South East Pacific EBUS. McGillicuddy et al (2007); Eden and Dietze (2009) and Anderson et al (2011) find significant biological impacts of the eddy-induced Ekman pumping. However, none of these studies focused on EBUS where the effect of the mesoscale eddies actively subduct nutrients and phytoplankton (Lathuilière et al, 2010; Gruber et al, 2011), in contrast with offshore, more oligotrophic regions. Consequently, the mesoscale air/sea coupling could certainly modify the horizontal and vertical transport of biogeochemicals tracers and further impact the ecosystem productivity.

Acknowledgements This work is part of V. Oerder's PhD thesis, sponsored by the Ministère de l'Enseignement Supérieur et de la Recherche. It is also part of the ANR project "PULSATION-11-MONU-010" and the LEFE/GMMC project "NEMPECH". Simulations were performed on the supercomputer Curie from the GENCI at the CEA (projects 2011040542, 2012061047 and 2014102286).

The authors want to thank Christophe Hourdin, Francoise Pinsard, Eric Maisonnave for their help in setting-up the coupled model NEMO-OASIS-WRF and Gurvan Madec, Swen Jullien, Hervé Giordani and Patrick Marchesiello for useful discussions. F. Lemarié acknowledges the support of the French LEFE/GMMC program through project SIMBAD. QSCAT WS data were provided by the CERSAT and are available online at ftp://ftp.ifremer.fr/ifremer/cersat/products/gridded/mwf-quikscat/data/. The OSCAR currents data were obtained from the NASA EOSDIS Physical Oceanography Distributed Active Archive Center (PO.DAAC) at the Jet Propulsion Laboratory, Pasadena, CA, https://podaac.jpl.nasa.gov/dataset/OSCAR_L4_OC_third-deg. Numerical data were obtained by model experiments described in Sect. 2.

References

Anderson LA, Jr DJM, Maltrud ME, Lima ID, Doney SC (2011) Impact of eddy–wind interaction on eddy demographics and phytoplankton community structure in a model of the North Atlantic Ocean. Dynamics of Atmospheres and Oceans 52(1–2):80–94, DOI {DOI}10.1016/j.dynatmoce.2011.01.003

Belmadani A, Echevin V, Dewitte B, Colas F (2012) Equatorially forced intraseasonal propagations along the Peru-Chile coast and their relation with the nearshore eddy activity in 1992–2000: A modeling study. J Geophys Res 117:C04,025, DOI 10.1029/2011JC007848

Blanke B, Delecluse P (1993) Variability of the Tropical Atlantic Ocean simulated by a general circulation model with two different mixed layer physics. J Phys Oceanogr 23:1363–1388, DOI 10.1175/1520-0485(1993)023<1363:VOTTAO>2.0.CO;2

Bonjean F, Lagerloef GSE (2002) Diagnostic model and analysis of the surface currents in the tropical Pacific Ocean. J Phys Oceanogr 32:2938–2954, DOI 10.1175/1520-0485(2002)032<2938:DMAAOT>2.0.CO;2

Bourras D, Reverdin G, Giordani H, Caniaux G (2004) Response of the atmospheric boundary layer to a mesoscale oceanic eddy in the northeast Atlantic. J Geophys Res 109:D18,114, DOI 10.1029/2004JD004799

Capet XJ, Marchesiello P, McWilliams JC (2004) Upwelling response to coastal wind profiles. Geophys Res Lett 31:L13,311, DOI 10.1029/2004GL020123.

Carr M, Kearns E (2003) Production regimes in four eastern boundary current systems. Deep Sea Res Part II 50(22–26):3199–3221, DOI 10.1016/j.dsr2.2003.07.015

Carton J, Giese B (2008) A reanalysis of ocean climate using simple ocean data assimilation (soda). Mon Weath Rev 136:2999–3017, DOI 10.1175/2007MWR1978.1

Chaigneau A, Gizolme A, Grados C (2008) Mesoscale eddies off Peru in altimeter records: Identification algorithms and eddy spatio-temporal patterns. Prog Oceanogr 79:106–119, DOI 10.1016/j.pocean.2008.10.013

Chaigneau A, Eldin G, Dewitte B (2009) Eddy activity in the four major upwelling systems from satellite altimetry (1992–2007). Prog Oceanogr 83:117–123, DOI 10.1016/j.pocean.2009.07.012

Chaigneau A, Texier ML, Eldin G, Grados C, Pizarro O (2011) Vertical structure of mesoscale eddies in the eastern South Pacific Ocean: A composite analysis from altimetry and Argo profiling floats. J Geophys Res 116:C11,025, DOI 10.1029/2011JC007134

Chaigneau A, Dominguez N, Eldin G, Vasquez L, Flores R, Grados C, Echevin V (2013) Near-coastal circulation in the Northern Humboldt Current System from shipboard ADCP data. J Geophys Res Oceans 118:5251–5266, DOI 10.1002/jgrc.20328

Chelton DB, Esbensen SK, Schlax MG, Thum N, Freilich MH, Wentz FJ, Gentemann CL, McPhaden MJ, Schopf PS (2001) Observations of coupling between surface wind stress and sea surface temperature in the Eastern Tropical Pacific. J Clim 14:1479–1498, DOI 10.1175/1520-0442(2001)014<1479:OOCBSW>2.0.CO;2

Chelton DB, Schlax MG, Freilich MH, Milliff RF (2004) Satellite measurements reveal persistent small-scale features in ocean winds. Science 303:978–983, DOI 10.1126/science.1091901

Colas F, McWilliams JC, Capet X, Kurian J (2012) Heat balance and eddies in the Peru-Chile current system. Clim Dyn 39(1-2):509–529, DOI 10.1007/s00382-011-1170-6

Colas F, Capet X, McWilliams J, Li Z (2013) Mesoscale eddy buoyancy flux and eddy-induced circulation in Eastern Boundary Currents. J Phys Oceanogr 43:1073–1095, DOI 10.1175/JPO-D-11-0241.1

Cornillon P, Park KA (2001) Warm core ring velocities inferred from NSCAT. Geophys Res Lett 28(4):575–578, DOI 10.1029/2000GL011487

Dee DP, et al (2011) The ERA-interim reanalysis: configuration and performance of the data assimilation system. Q J R Meteorol Soc 137:553–597, DOI 10.1002/qj.828

Dewar WK, Flierl GR (1987) Some effects of the wind on rings. J Phys Oceanogr 17:1653–1667, DOI 10.1175/1520-0485(1987)017<1653:SEOTWO>2.0.CO;2

Duhaut THA, Straub DN (2006) Wind stress dependence on ocean surface velocity: Implications for mechanical energy input to ocean circulation. J Phys Oceanogr 36:202–211, DOI 10.1175/JPO2842.1

Dunbar R, Lungu T, Weiss B, Stiles B, Huddleston J, Callahan P, Shirtliffe G, Perry K, Hsu C, Mears C, Wentz F, Smith D (2006) QuikSCAT science data product user manual, version 3.0. JPL Document D-18053 - Rev A Jet Propulsion Laboratory, Pasadena, CA

Eden C, Dietze H (2009) Effects of mesoscale eddy/wind interactions on biological new production and eddy kinetic energy. J Geophys Res: Oceans 114(C5), DOI 10.1029/2008JC005129, c05023

Engedahl H (1995) Use of the flow relaxation scheme in a three-dimensional baroclinic ocean model with realistic topography. Tellus A 47:365–382, DOI 10.1034/j.1600-0870.1995.t01-2-00006.x

Farrow DE, Stevens DP (1995) A new tracer advection scheme for Bryan and Cox type ocean general circulation models. J Phys Oceanogr 25:1731–1741, DOI 10.1175/1520-0485(1995)025<1731:ANTASF>2.0.CO;2

Flather RA (1976) A tidal model of the northwest European continental shelf. Memoires de la Societe Royale de Sciences de Liege 6:141–164

Frenger I, Gruber N, Knutti R, Münnich M (2013) Imprint of Southern Ocean eddies on winds, clouds and rainfall. Nat Geosci 6:608–612, DOI 10.1038/ngeo1863

Gaube P, Chelton DB, Samelson RM, Schlax MG, O'Neill LW (2015) Satellite observations of mesoscale eddy-induced Ekman pumping. J Phys Oceanogr 45:104–132, DOI 10.1175/JPO-D-14-0032.1

Gruber N, Lachkar Z, Frenzel H, Marchesiello P, Münnich M, McWilliams JC, Nagai T, Plattner GK (2011) Eddy-induced reduction of biological production in Eastern Boundary Upwelling Systems. Nat Geosci 4:787–792, DOI 10.1038/ngeo1273

Haney R, Hale RA, Dietrich DE (2001) Offshore propagation of eddy kinetic energy in the California Current. J Geophys Res 106, C6:11,709–11,717, DOI 10.1029/2000JC000433

Isern-Fontanet J, Garcia-Ladona J, Font J (2003) Identification of marine eddies from altimetric maps. J Atmos Ocean Technol 20:772–778, DOI 10.1175/1520-0426(2003)20<772:IOMEFA>2.0.CO;2

Kurian J, Colas F, Capet X, McWilliams J, Chelton D (2011) On the properties of eddies in the California Current System. J Geophys Res 116:C08,027, DOI 10.1029/2010JC006895

Lathuilière C, Echevin V, Lévy M, Madec G (2010) On the role of the mesoscale circulation on an idealized coastal upwelling ecosystem. J Geophys Res 115:C09,018, DOI 10.1029/2009JC005827

Lemarié F (2015) Numerical modification of atmospheric models to include the feedback of oceanic currents on air-sea fluxes in ocean-atmosphere coupled models. Technical Report RT-464, INRIA Grenoble - Rhône-Alpes, https://hal.inria.fr/hal-01184711/file/RT-464.pdf

Liang JH, McWilliams JC, Kurian J, Colas F, Wang P, Uchiyama Y (2012) Mesoscale variability in the northeastern tropical pacific: Forcing mechanisms and eddy properties. J Geophys Res 117(C7), DOI 10.1029/2012JC008008

Liu WT, Zhang A, Bishop JKB (1994) Evaporation and solar irradiance as regulators of sea surface temperature in annual and interannual changes. J Geophys Res 99:12,623–12,637, DOI 10.1029/94JC00604

Lévy M, Estubier A, Madec G (2001) Choice of an advection scheme for biogeochemical models. Geophys Res Let 28:3725–3728, DOI : 10.1029/2001GL012947

Madec G (2008) NEMO ocean engine. Note du Pole de modélisation, Institut Pierre-Simon Laplace (IPSL) 27:ISSN No 1288–1619

Marchesiello P, McWilliams JC, Shchepetkin A (2003) Equilibrium structure and dynamics of the California Current System. J Phys Oceanogr 33:753–783, DOI 10.1175/1520-0485(2003)33<753:ESADOT>2.0.CO;2

McGillicuddy DJ, Anderson LA, Bates2 NR, Bibby T, Buesseler KO, Carlson CA, Davis1 CS, Ewart C, Falkowski PG, Goldthwait SA, Hansell DA, Jenkins WJ, Johnson R, Kosnyrev VK, Ledwell JR, Li QP, Siegel DA, Steinberg DK (2007) Eddy/wind interactions stimulate extraordinary mid-ocean plankton blooms. Science 316:5827:1021–1026, DOI 10.1126/science.1136256

Munday D, Zhai X (2015) Sensitivity of southern ocean circulation to wind stress changes: Role of relative wind stress. Ocean Modelling 95:15–24, DOI 10.1016/j.ocemod.2015.08.004

Nakanishi M, Niino H (2009) Development of an improved turbulence closure model for the atmospheric boundary layer. J Meteorol Soc Jap 87:895–912, DOI 10.2151/jmsj.87.895

Oerder V, Colas F, Echevin V, Codron F, Tam J, Belmadani A (2015) Peru-Chile upwelling dynamics under climate change. J Geophys Res: Oceans 120(2):1152–1172, DOI 10.1002/2014JC010299

Oerder V, Colas F, Echevin V, Masson S, Hourdin C, Jullien S, Madec G, Lemarié F (2016) Mesoscale sst–wind stress coupling in the peru–chile current system: Which mechanisms drive its seasonal variability? Climate Dynamics pp 1–22, DOI 10.1007/s00382-015-2965-7

Oerder V, Colas F, Echevin V, Masson S, Lemarié F (2017) Impacts of the mesos1 cale ocean-atmosphere coupling on the peru-chile ocean dynamics : impact of the sst-induced atmospheric response. in prep

O'Neill LW, Chelton DB, Esbensen SK (2010a) The effects of SST-induced surface wind speed and direction gradients on midlatitude surface vorticity and divergence. J Clim 23:255–281, DOI 10.1175/2009JCLI2613.1

O'Neill LW, Esbensen SK, Thum N, Samelson RM, Chelton DB (2010b) Dynamical analysis of the boundary layer and surface wind responses to mesoscale SST perturbations. J Clim 23:559–581, DOI 10.1175/2009JCLI2662.1

Pegliasco C, Chaigneau A, Morrow R (2015) Main eddy vertical structures observed in the four major Eastern Boundary Upwelling systems. J Geophys Res Oceans 120, DOI 10.1002/2015JC010950

Renault L, Molemaker MJ, McWilliams JC, Shchepetkin AF, Lemarié F, Chelton D, Illig S, Hall A (2016) Modulation of wind work by oceanic current interaction with the Atmosphere. J Phys Oceanogr 46(6):1685–1704, DOI 10.1175/JPO-D-15-0232.1

Samelson R, Schlax M, Chelton D (2014) Randomness, symmetry, and scaling of mesoscale eddy life cycles. J Phys Oceanogr 44:1012–1029, DOI 10.1175/JPO-D-13-0161.1.

Seo H, Miller AJ, Norris JR (2015) Eddy-wind interaction in the California Current System: dynamics and impacts. J Phys Oceanogr 46, 439–459, DOI 10.1175/JPO-D-15-0086.1

Skamarock W, Klemp J (2008) A time-split nonhydrostatic atmospheric model for weather research and forecasting applications. J Comp Phys 227:3465–3485, DOI 10.1016/j.jcp.2007.01.037

Small RJ, deSzoeke SP, Xie SP, O'Neill L, Seo H, Song Q, Cornillon P, Spall M, Minobe S (2008) Air–sea interaction over ocean fronts and eddies. Dyn Atmos Oceans 45:274–319, DOI 10.1016/j.dynatmoce.2008.01.001

Strub PT, Mesias JM, Montecino V, Ruttlant J, Salinas S (1998) Coastal ocean circulation off Western South America. The Sea vol 11, chap 10:29–67

Valcke S, Craig T, Coquart L (2013) OASIS3-MCT user guide, OASIS3-MCT 2.0. Tech. rep., CERFACS/CNRS SUC URA No 1875

Wang W, Huang R (2004) Wind energy input to the Ekman layer. J Phys Oceanogr 34:1267–1275, DOI 10.1175/1520-0485(2004)034<1267:WEITTE>2.0.CO;2

Webb D, de Cuevas B, Richmond C (1998) Improved advection schemes for ocean models. J Atmos Ocean Technol 15(5):1171–1187, DOI 10.1175/1520-0426(1998)015<1171:IASFOM>2.0.CO;2

Wunsch C (1998) The work done by the wind on the oceanic general circulation. J Phys Oceanogr 28:2332–2340, DOI 10.1175/1520-0485(1998)028<2332:TWDBTW>2.0.CO;2

Xie SP (2004) Satellite observations of cool ocean–atmosphere interaction. Bull Am Meteorol Soc 85:195–208, DOI 10.1175/BAMS-85-2-195

Zhai X, Greatbatch RJ (2007) Wind work in a model of the northwest Atlantic ocean. Geophys Res Lett 34:L04,606, DOI 10.1029/2006GL028907

Tables

a)

	Abs	Rel
Number of cyclones detected	2082	1955
Mean radius	46 km	44 km
Mean lifetime	41 days	35 days
Number of cyclones with a lifetime longer than 40 days	578 (28 % of the total)	492 (25 % of the total)

b)

	Abs	Rel
Number of anticyclones detected	2299	2022
Mean radius	47 km	45 km
Mean lifetime	34 days	30 days
Number of anticyclones with a lifetime longer than 40 days	520 (23 % of the total)	383 (19 % of the total)
Number of subsurface anticyclones	1133 (49 % of the total)	1015 (50 % of the total)

Table 1: Characteristics of the (a) cyclones and (b) anticyclones detected in the two simulations

Figures

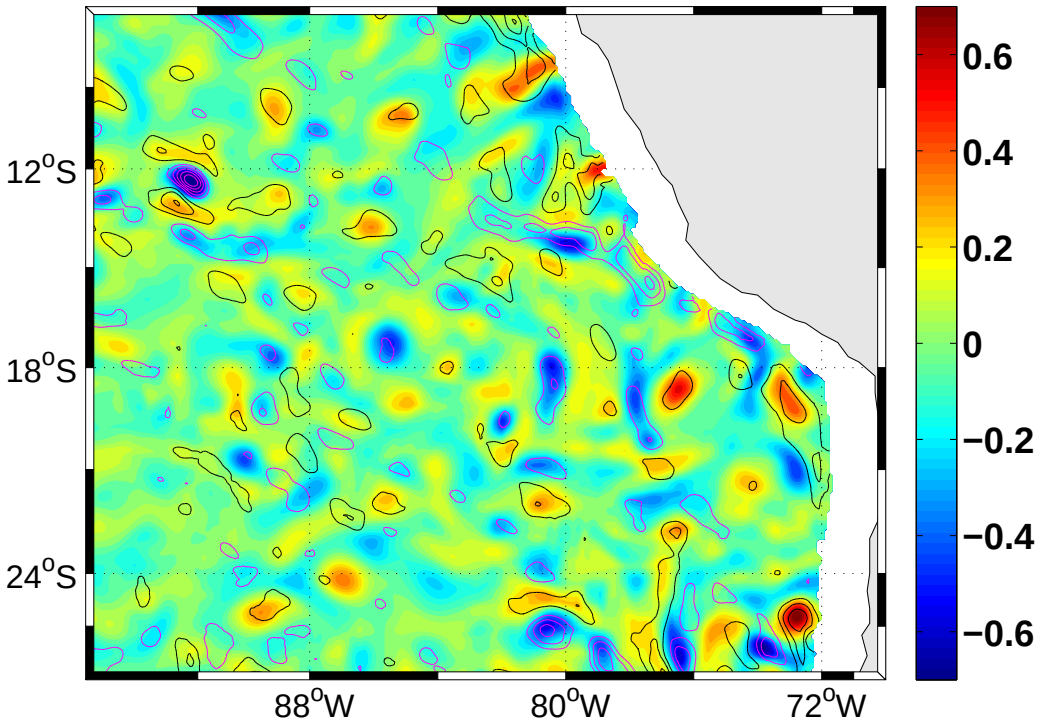

Fig. 1: Mesoscale anomalies of the surface current vorticity (colors, in 10^{-5} s^{-1}) and curl$(\overrightarrow{\tau_s})_{res}$ (contours, with a 3 10^{-8} N m^{-3} interval, black line is for negative values and magenta line for positive values), monthly-mean for July 2004 in Rel coupled simulation. Mesoscale anomalies are computed using two Gaussian spatial filters with 30 km and 150 km standard deviations to remove the large and small scale structures.

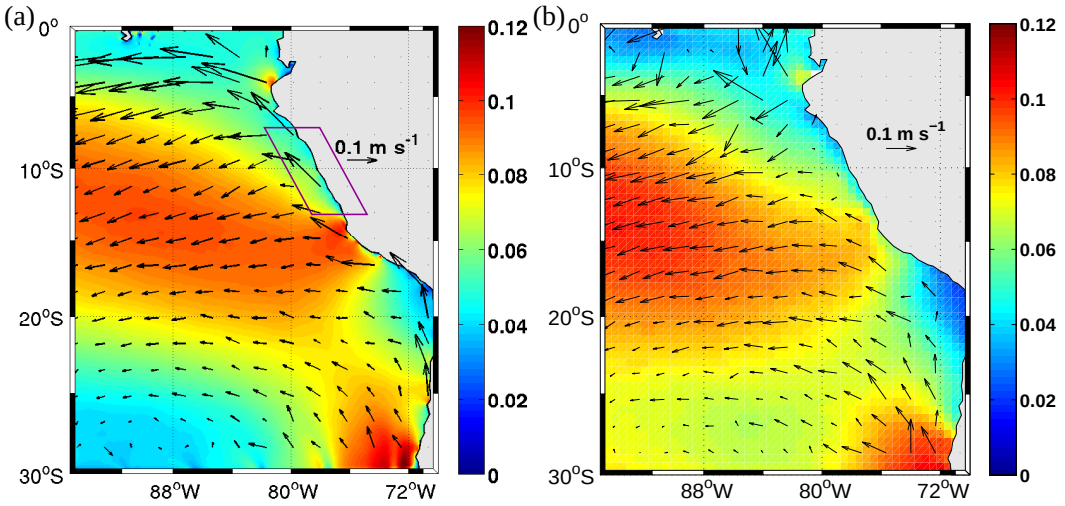

Fig. 2: 2003-2008 mean wind stress intensity (colors, in N m^{-2}) and surface current (arrows) for (a) Rel simulation and (b) observations from QSCAT wind data (Dunbar et al, 2006) and Ocean Surface Current Analysis–Real Time (OSCAR) product (Bonjean and Lagerloef, 2002). A 0.015 N m^{-2} constant bias has been added to the model wind stress intensity. The 7 °S - 13 °S coastal region is indicated by the magenta box

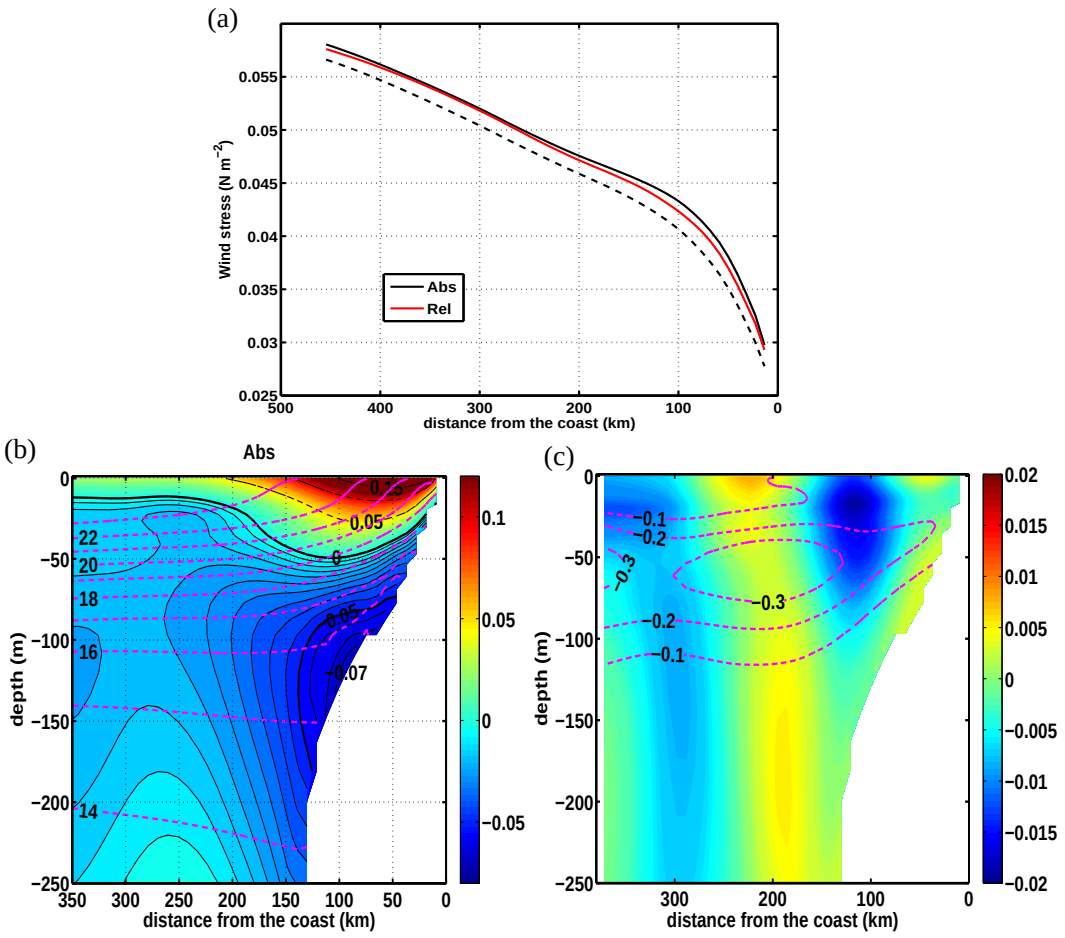

Fig. 3: (a) Mean wind stress intensity (N m^{-2}) with respect to the distance from the coast (in km) for Abs (black plain line) and Rel (red plain line) simulations. The black dotted line represents a wind stress computed offline following equation (2) and using $\overrightarrow{v_s^a}$ and $\overrightarrow{v_1^o}$ from Abs. (b) Mean alongshore current velocities (shading, in m s^{-1}) and temperature (dashed magenta line, in ° C, with a 1 °C interval) for Abs. Thin plain black velocity contour interval is 0.5 cm s^{-1} and black bold contours marks 0 and -5 cm s^{-1}. Thin dotted black velocity contour interval is 5 cm s^{-1} (c) Difference between the mean alongshore current velocities (shading, in m s^{-1}) in Rel and in Abs. Contours marks the temperature differences (in °C) with a 0.1 °C interval. All fields are averaged over the 2003-2008 period and from 7° S to 13° S.

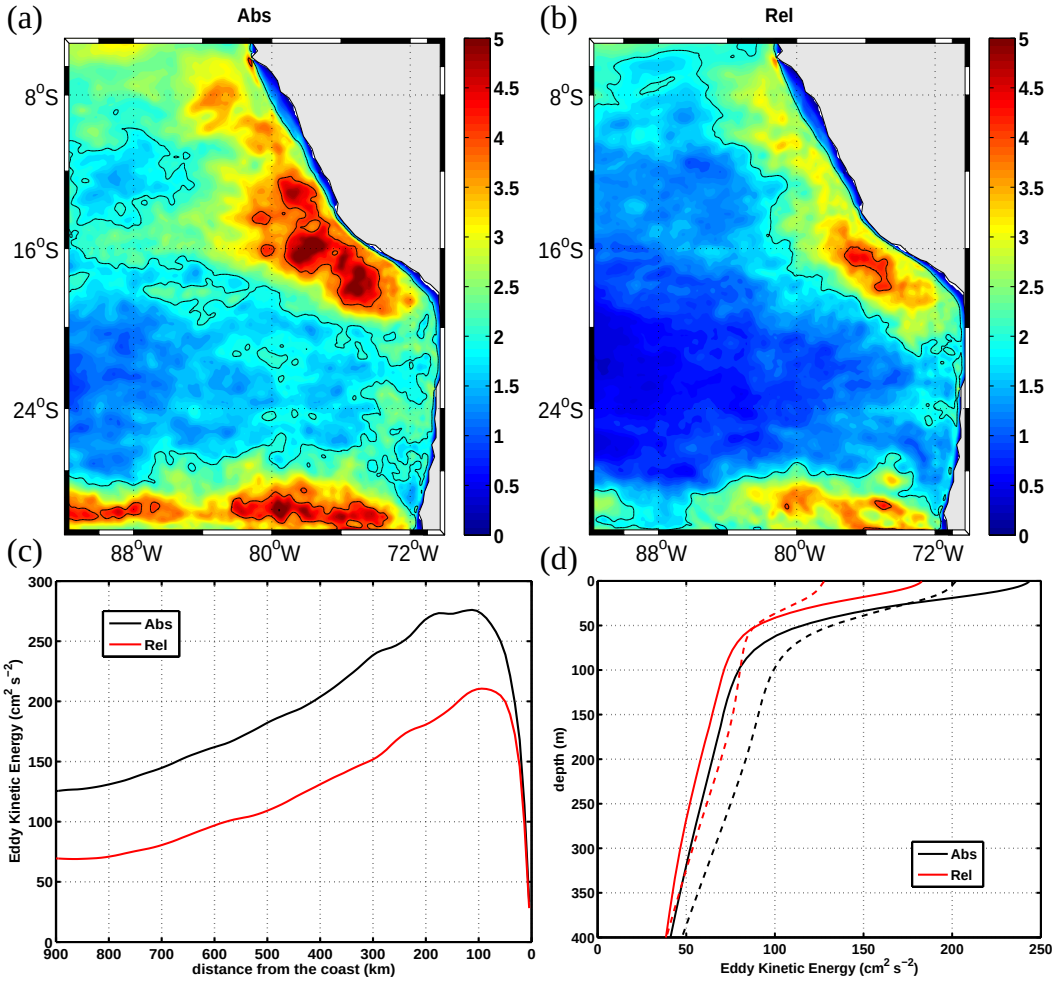

Fig. 4: (a)-(b) 2003-2008 mean eddy kinetic energy (EKE) integrated from the surface to 400 m depth (in m^3 s^{-2}), in Abs and Rel simulations. (c) 2003-2008 mean surface EKE (cm^2 s^{-2}), averaged between 7 °S and 13 °S, with respect to the distance from the coast (in km). (d) EKE vertical profile (cm^2 s^{-2}), averaged over the 2003-2008 period, from 7 °S to 13 °S, and from 0 to 200 km offshore (plain line) or from 300 to 450 km offshore (dotted line). Red (black) lines are for Rel (Abs, respectively).

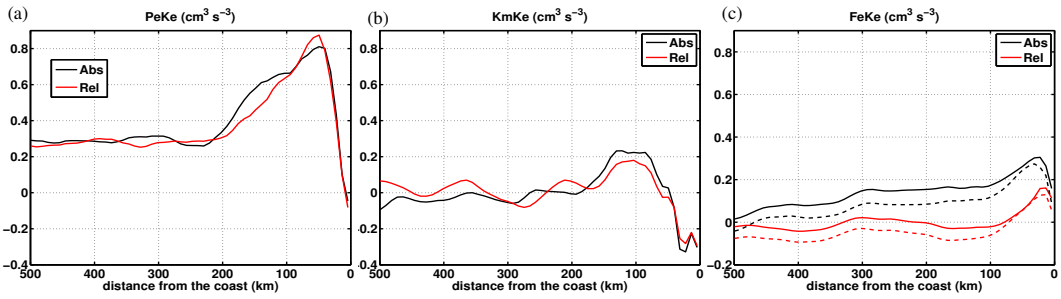

Fig. 5: EKE generation terms (in cm^3 s^{-3}) with respect to the distance from the coast (in km), averaged over the 2003-2008 period, from 7 °S to 27 °S for Abs (black) and Rel (red). (a) P_eK_e term, (b) K_mK_e term (c) F_eK_e (plain line) and F_eK_{eg} (dotted line) term.

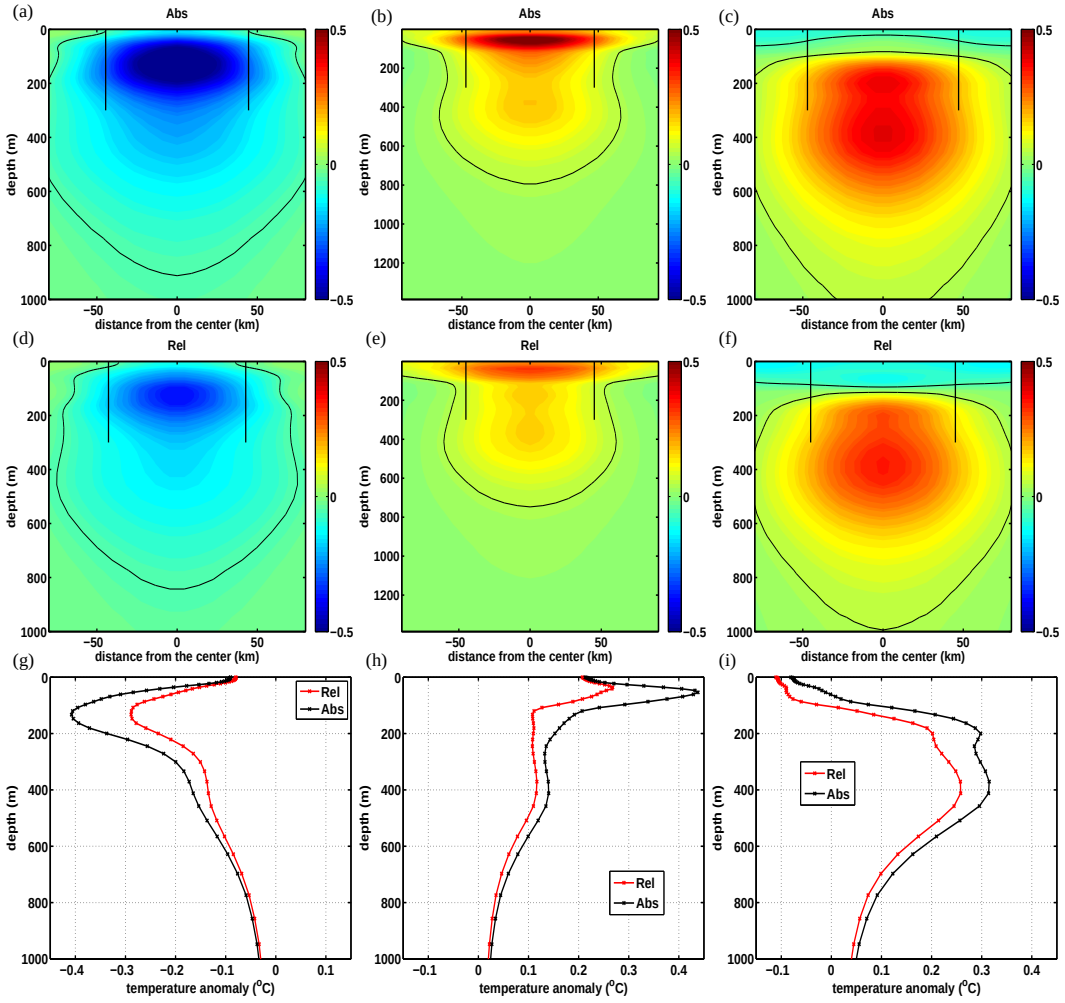

Fig. 6: Vertical structure of the temperature anomaly (in °C) composite in (a) the cyclones detected in Abs, (b) the surface and (c) subsurface anticyclones detected in Abs, (d) the cyclones detected in Rel, (e) the surface and (f) subsurface anticyclones detected in Rel. Thin line marks the 0.05 °C contour and the bold vertical lines marks the mean eddy diameter. A radial average has been performed on the 3D composites to obtain the mean vertical structure. (g)-(i) : mean vertical profile of the temperature anomaly (in °C) in (g) the cyclones and (h) the surface and (i) subsurface anticyclones. Red (black) lines are for Rel (Abs, respectively).

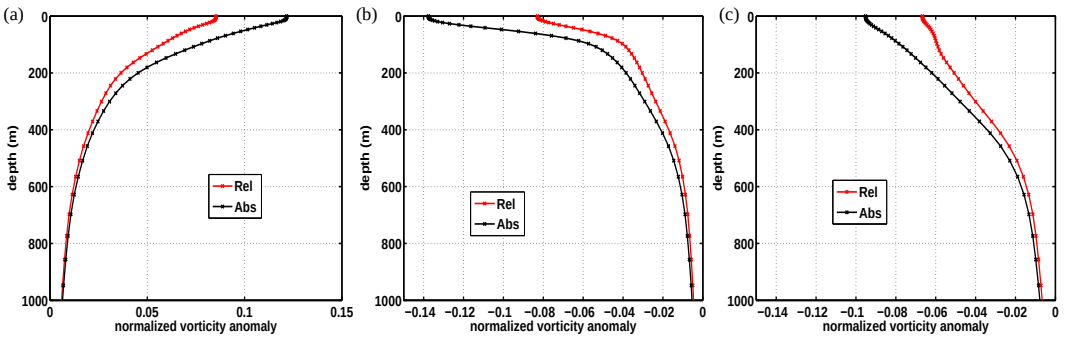

Fig. 7: Mean vertical profile of $\frac{\zeta}{f}$ anomaly in (a) the cyclones and (b) the surface and (c) subsurface anticyclones. Red (black) lines are for Rel (Abs, respectively).

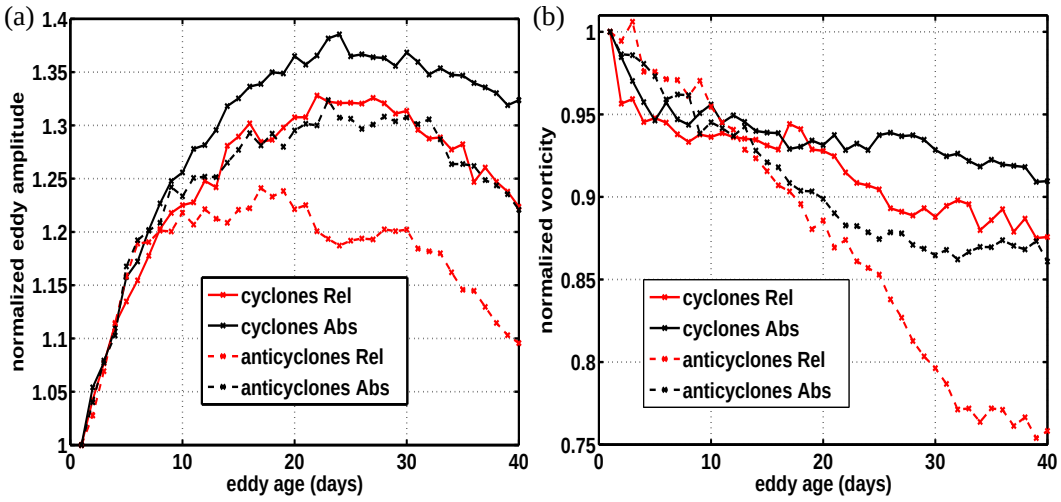

Fig. 8: Evolution of the (a) eddy composite amplitude and (b) the mean vorticity in Abs (black lines) and Rel (red lines) for the cyclones (plain lines) and anticyclones (dotted lines). For each day after its detection, the eddy amplitude is computed from the daily SSH anomaly composite as the difference between the SSH extremum and the mean SSH anomaly on the circle fitting the eddy (see Sec. 2.2). The amplitude and vorticity are normalized by the values at the first detection day.

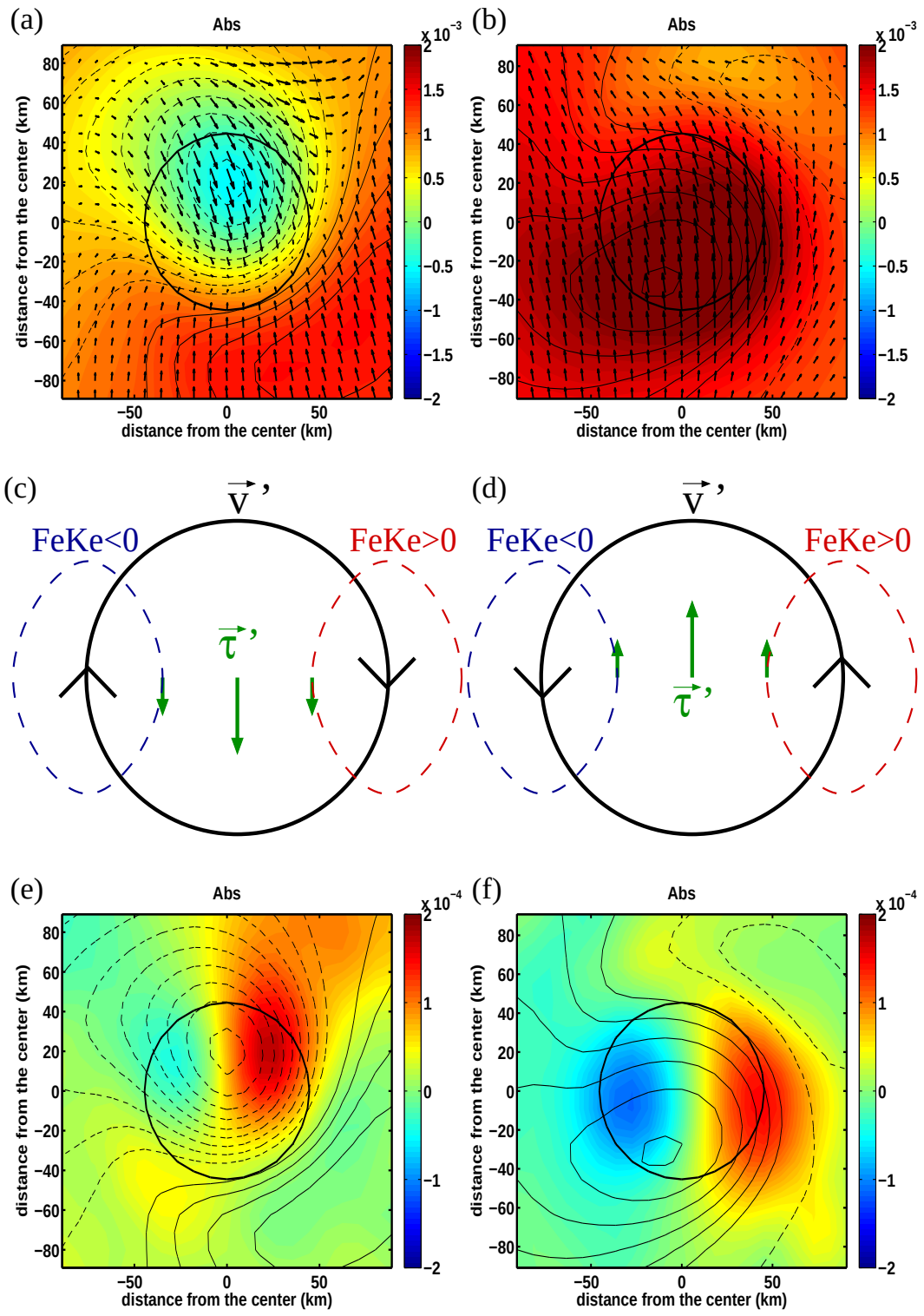

Fig. 9: Composites computed using Abs simulation. (a)-(b) Composites of the wind stress intensity anomaly (colors, in N m^{-3}) above the (a) cyclones and (b) anticyclones. Composites of the wind stress anomaly are represented by the arrows and the thin black contours represent the composites of the SST anomaly with a 0.02 °C interval, plain (dotted) lines are for positive (negative, respectively) values. (c)-(d) Scheme of the wind work associated to the SST-induced wind stress anomaly on a (c) cyclone and (d) an anticyclone. The current anomaly is represented by the black arrows, the wind stress anomaly is represented by the green arrows and the regions with positive (negative) wind work are marked with red (blue, respectively) dotted lines. (e)-(f) Composites of the wind work (m^3 s^{-3}) on the (e) cyclones and (f) anticyclones in colors. The thin black contours represent the composites of the SST anomaly with a 0.02 °C interval, plain (dotted) lines are for positive (negative, respectively) values. Black circles represent the mean eddy radius.

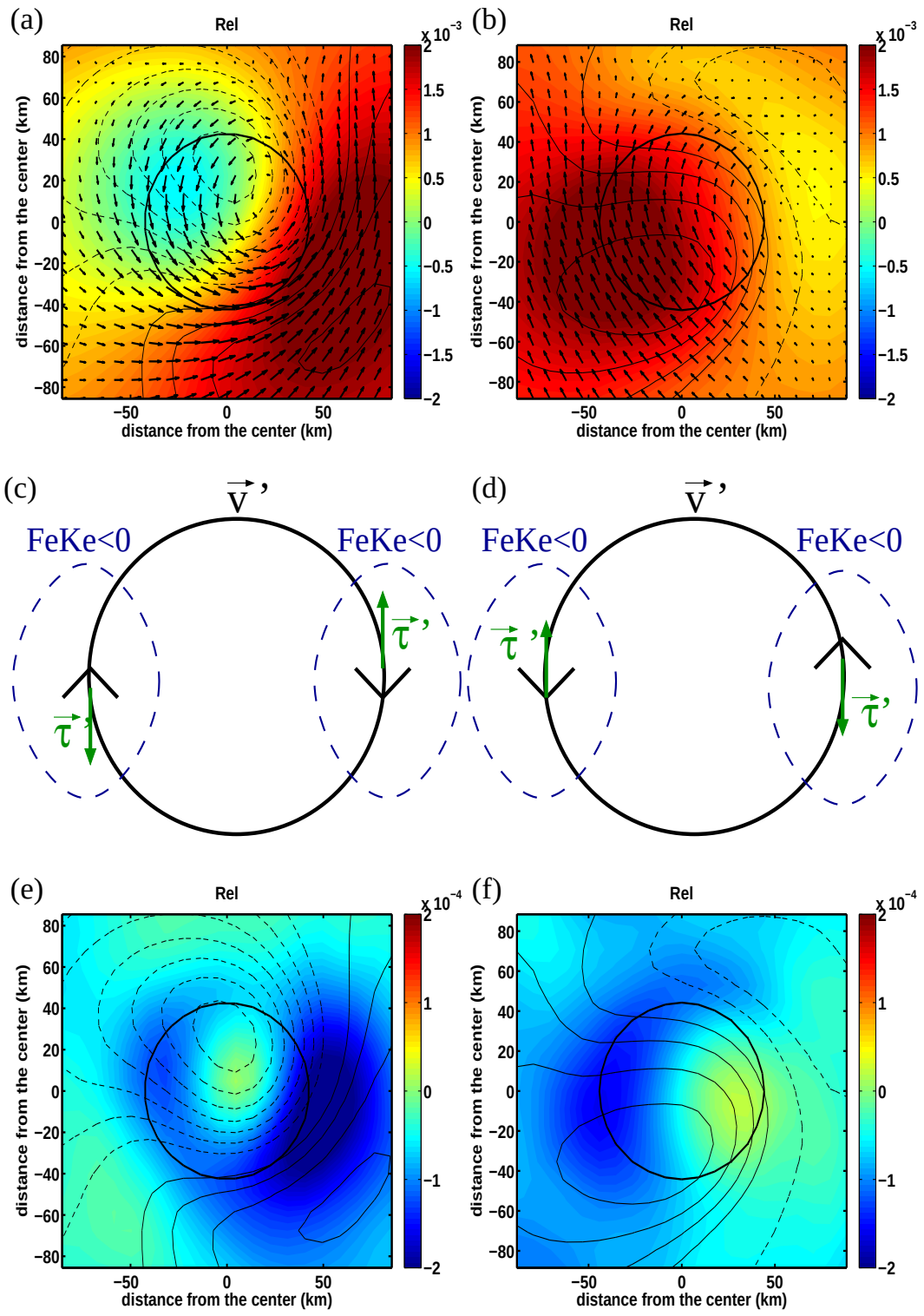

Fig. 10: Same as Fig. 9 but for Rel.

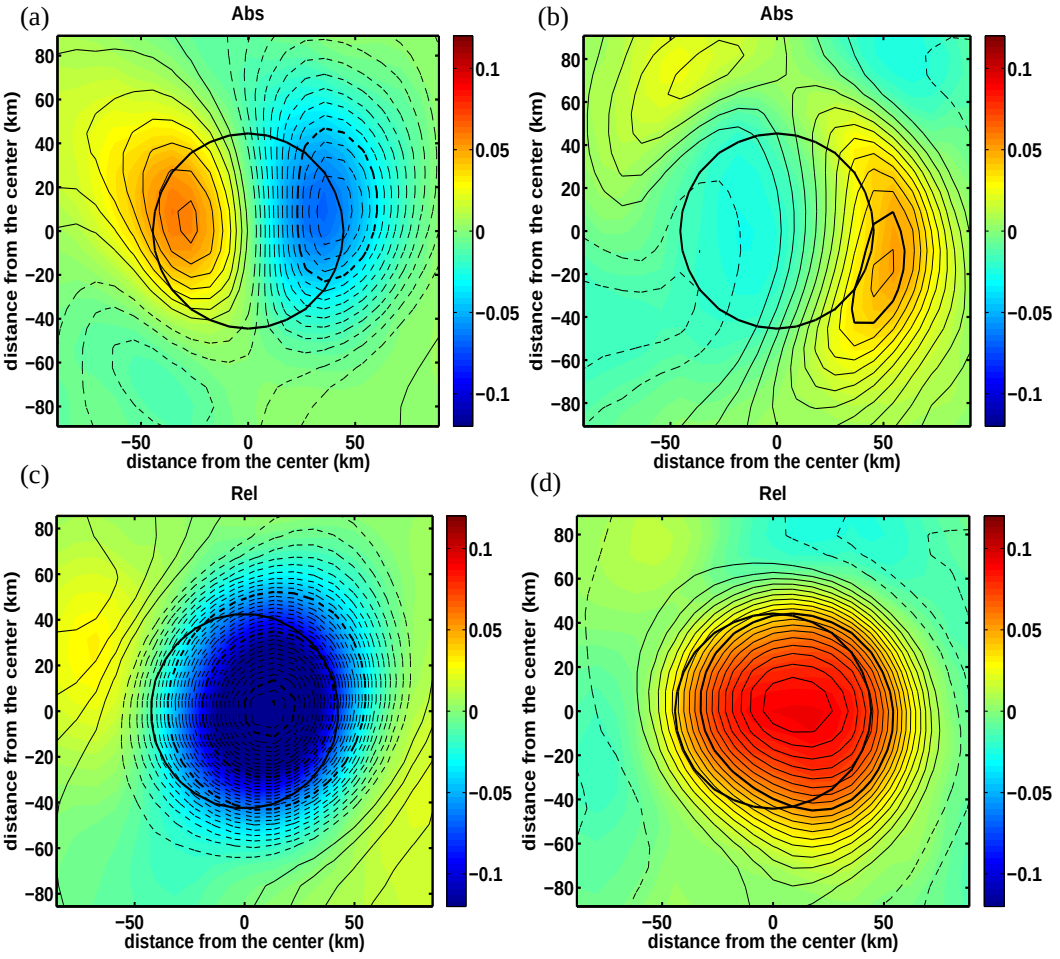

Fig. 11: Ekman pumping W_{Ek} (in m day^{-1}) composite in (a) the cyclones detected in Abs, (b) the anticyclones detected in Abs, (c) the cyclones detected in Rel, and (d) the anticyclones detected in Rel. Black thin (bold) contours represents $s_1 grad_{cr}(SST)$ in (a), (b) and $s_1 grad_{cr}(SST) + s_2 curl(\overrightarrow{v_1^{\partial}}')$ in (c), (d), with a 0.005 (0.05, respectively) m day^{-1} interval. Dotted (plain) contours are for negative (positive, respectively) values. Black circles represent the mean eddy radius.

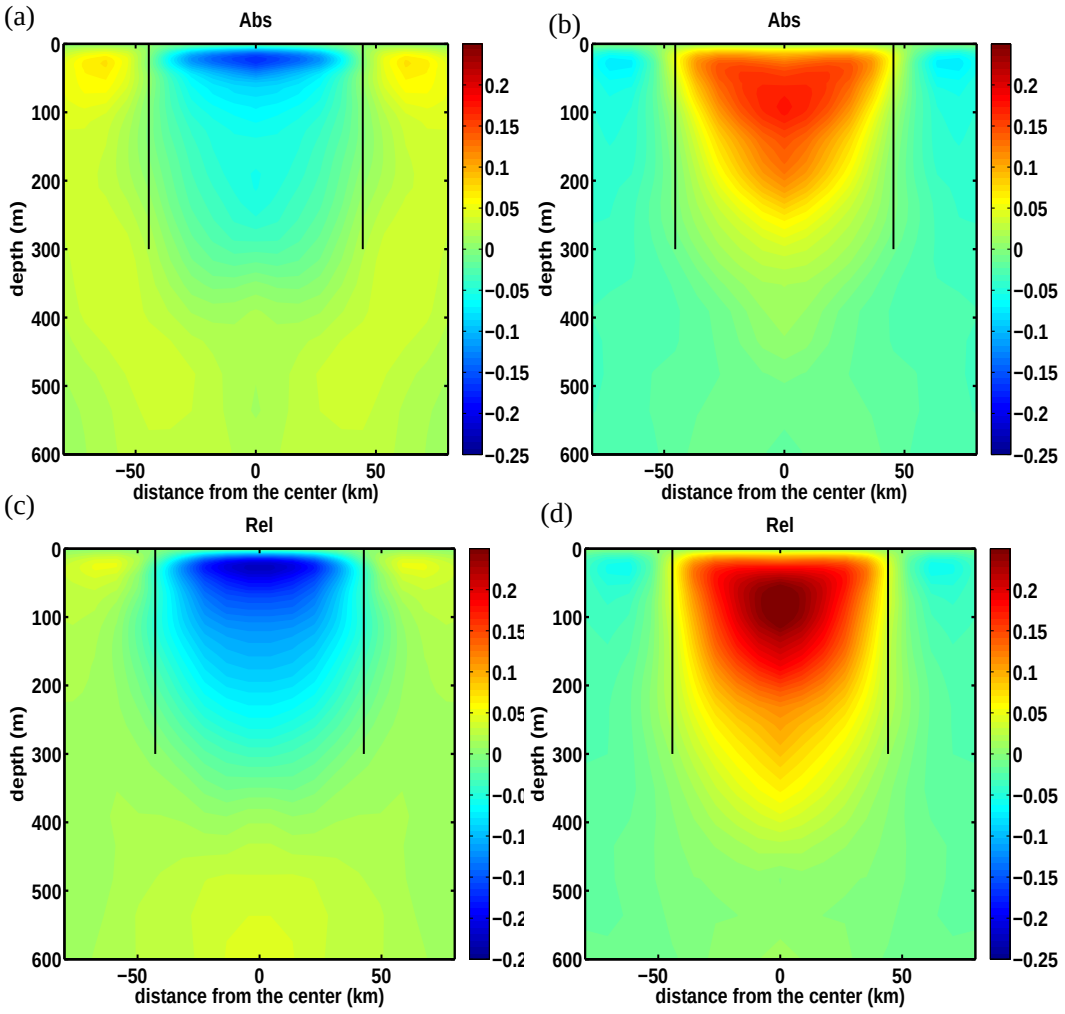

Fig. 12: Vertical structure of the vertical velocity anomaly (in m day^{-1}) composite in (a) the cyclones detected in Abs, (b) the anticyclones detected in Abs, (c) the cyclones detected in Rel, and (d) the anticyclones detected in Rel. The bold vertical lines marks the mean eddy diameter. A radial average has been performed on the 3D composites to obtain the mean vertical structure.